

Micromagnetic view on ultrafast magnon generation by femtosecond spin current pulses

Henning Ulrichs*

I. Physical Institute, Georg-August University of Göttingen, Friedrich-Hund-Platz 1, 37077 Göttingen, Germany

Ilya Razdolski

Physical Chemistry Department, Fritz Haber Institute of the Max Planck Society, Faradayweg 4-6, 14195 Berlin, Germany



(Received 26 January 2018; revised manuscript received 2 July 2018; published 27 August 2018)

In this paper, we discuss a micromagnetic modeling approach to describe the ultrafast spin-transfer torque excitation of coherent and incoherent magnons on the nanoscale. Implementing the action of a femtosecond spin current pulse entering an orthogonally magnetized thin ferromagnetic film, we reproduce recent experimental results and reveal the factors responsible for the unequal excitation efficiency of various spin waves. Our findings are in an excellent agreement with the results of an analytical description of spin-wave excitation based on classical kinetic equations. Furthermore, we suggest an experimental design allowing for the excitation of laterally propagating spin waves beyond the optical diffraction limit. Our findings demonstrate that the classical micromagnetic picture retains its predictive and interpretative power for modeling the reaction of the magnetization on dynamical stimuli that reside on femtosecond temporal and nanometer spatial scales.

DOI: [10.1103/PhysRevB.98.054429](https://doi.org/10.1103/PhysRevB.98.054429)

I. INTRODUCTION

Stimulated by the seminal experiment by Beaurepaire *et al.* [1] and the quest for ultrafast optomagnetic recording, an immense amount of knowledge on the incoherent laser-induced spin dynamics (i.e., ultrafast demagnetization) in a large variety of materials has been accumulated over the years [2]. Simultaneously, femtosecond optical excitations of coherent spin dynamics were discovered [3,4], encompassing an extremely broad range of timescales that are governed by the intrinsic properties of magnetic systems. The temporal limitation for the excited spin modes is often pertinent to the pulse duration of the light source, typically on the order of 10–100 fs. However, the spectrum of the accessible inhomogeneous (with nonzero wave vector k) spin-wave modes is governed by the spatial inhomogeneity scale of the excitation. In other words, on top of the temporal requirements, nonuniform spin-wave modes can only be generated if their wave vectors k are contained in the spectrum of the spatially inhomogeneous stimulus. For the excitation with visible (VIS) or near-infrared (NIR) light, the optical penetration depth $\delta \approx 10\text{--}15$ nm serves as a good estimation for the excitation limit of perpendicular spin waves in metallic media [5]. Optical excitation of the in-plane propagating spin waves is even more restrictive, as the allowed k values are governed by the diffraction-limited beam spot size ($\gtrsim 10^3\text{--}10^4$ nm) [6,7].

Yet, in recent experiments, a strong interfacial localization of the spin-transfer torque exerted by spin polarized currents enabled the excitation of spin waves with much larger wave vectors [8,9]. In particular, perpendicular standing spin waves (PSSW) with $f = 0.55$ THz and $k \sim 1$ nm⁻¹ have been detected [8]. The wavelengths of these excitations approach the exchange length l_{ex} (a few nanometers in Fe [10]), where

macroscopic spin models are likely to break down [11]. Enabling the expansion of ultrafast photomagnonics [12,13] onto the nanometer scale, these findings simultaneously question the applicability of conventional modeling of spin dynamics in these extreme conditions.

For conventional magnonics, micromagnetic simulation is an indispensable tool for both prediction, and interpretation of static and dynamic magnetic properties [14–20]. In this paper, we show that the micromagnetic modeling approach is also suitable for ultrafast processes on nanometer scales [8,9,21,22]. In particular, we set up a micromagnetic model to first reproduce the recent experimental findings [8] of ultrafast optical magnon generation. In this study, Fe/Au/Fe trilayers were optically pumped from one side, generating a superdiffusive [22] spin current pulse that traverses the Au spacer and then interacts with the second Fe layer, resulting in the excitation of high-frequency spin dynamics in the terahertz (THz) domain. Here we develop a micromagnetic model featuring ultrafast spin-transfer torque perturbation and verify that it can accurately reproduce the above mentioned spectral features of experimentally observed spin dynamics. We further identify important factors governing the excitation efficiency and energy transfer into the PSSW modes in thin ferromagnetic films. Complementing a recent theoretical work [23] on laser-generated superdiffusive spin transport in noncollinear spin valve systems and resulting macrospin dynamics in ferromagnets, our results open the door to understanding spin current-driven magnetism on the nanoscale. Later on, we include thermally activated, incoherent magnetic fluctuations in the model, and show that ultrafast spin currents can effectively cool or heat such thermal magnon ensembles, in agreement with experimental observations on slower timescales [24]. In the outlook, we outline the topological possibilities for the spin current-mediated generation of in-plane propagating, large- k spin waves beyond the optical diffraction limit.

*hulrich@gwdg.de

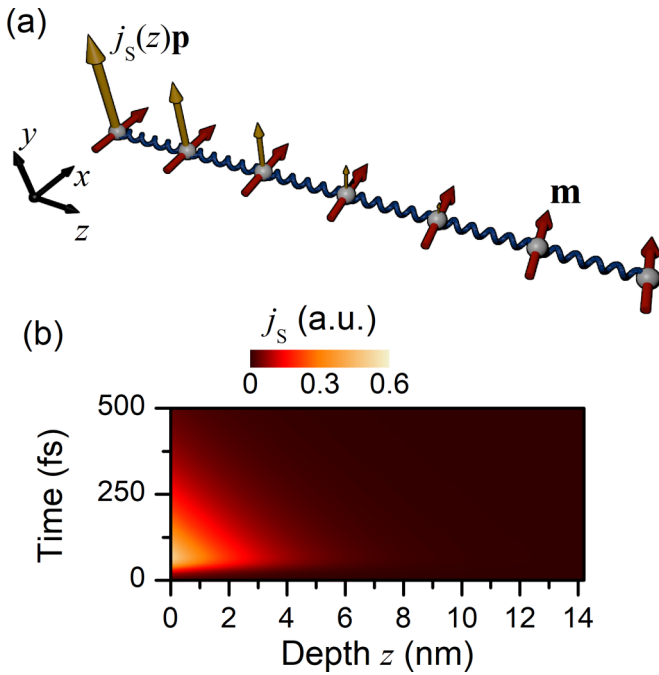


FIG. 1. Model details. (a) Sketch of the micromagnetic model. Besides incorporating the spin current, the model optionally includes thermal fluctuations. (b) Spatiotemporal dependence of the spin current entering the film, assuming $\lambda_{\text{STT}} = 2$ nm.

II. MODEL DETAILS

Our model is visualized in Fig. 1(a). It consists of a single ferromagnetic layer of Fe, with a thickness of $d = 14.2$ nm. We take as material parameters a saturation magnetization of $\mu_0 M_0 = 2.1$ T, an exchange constant of $A_{\text{ex}} = 19$ pJ/m (corresponding to the exchange stiffness $D = 280 \text{ \AA}^2 \text{ meV}$ in Fe from Ref. [25]), and a uniaxial anisotropy along \mathbf{x} with strength $K_u = 45956 \text{ J/m}^3$, and assume a Gilbert damping factor of $\alpha = 0.008$.

For the demonstration of coherent magnon generation, we simulate a cube of size $1.16 \times 1.16 \times 14.2 \text{ nm}^3$ subdivided into $N_x \times N_y \times N_z = 2 \times 2 \times 24$ cells. Periodic boundary conditions in \mathbf{x} and \mathbf{y} direction enlarge this cube into an infinitely extended film. Micromagnetism as a classical field theory can describe spin-wave dynamics for wavelengths larger than a few nanometers. The wavelength has to significantly exceed the atomic lattice constant, which is for iron about 0.3 nm. Note that using mesh cells with comparable size is not an attempt to claim the applicability of our micromagnetic approach on this atomic scale. Instead, this is done in order to smoothly describe spin waves on the somewhat larger scale, that is, with wavelengths of several nanometers. As such, in this work, we intentionally reach and explore the limits of micromagnetism, whereas going further beyond this limit requires other models [26].

For the demonstration of incoherent magnon creation and annihilation, we simulate a larger cube of size $150 \times 150 \times 14.2 \text{ nm}^3$ subdivided into $N_x \times N_y \times N_z = 256 \times 256 \times 24$ cells. Note that in this case, an additional magnetic field representing thermal fluctuations is switched on [27]. Further temperature dependencies of the material parameters, like, e.g.,

the saturation magnetization M_0 are neglected, because we stay far enough away from the Curie temperature of iron (~ 1000 K).

The spin current j_s with polarization \mathbf{p} enters the system at $z = 0$, and has the following empirical spatiotemporal form:

$$j_s = \frac{\hbar}{2e} j_0 e^{-z/\lambda_{\text{STT}}} \frac{e^{-t/\tau_2}}{1 + e^{-(t-t_0)/\tau_1}}. \quad (1)$$

Here the penetration depth of the spin current is $\lambda_{\text{STT}} = 2$ nm, as estimated in Ref. [8], and the temporal profile of the spin current pulse [Fig. 1(b)] is approximated with an analytic function (1) with $t_0 = 50$ fs, $\tau_1 = 10$ fs, and $\tau_2 = 150$ fs. The degree of spin polarization is set to 100 %, following the results of Ref. [28] and, most importantly, the spirit of the nonthermal mechanism of spin current generation at noble metal/ferromagnet interfaces discussed in that work. Note that in Eq. (1) we neglect the actual propagation of the spin current pulse inside the Fe film with the Fermi velocity ~ 1 nm/fs, due to the fact that this speed is much larger than the phase and group velocities of the involved magnons. We use the software package MUMAX³ (Ref. [27]) to model the effect of a spin current pulse on the local magnetization inside the Fe film by augmenting the Landau-Lifshitz-Gilbert equation with the spin-transfer torque (STT) term τ_{STT} proposed by Slonczewski [29]:

$$\tau_{\text{STT}} = \gamma \frac{N_z}{d\mu_0 M_0} j_s \mathbf{M} \times \mathbf{M} \times \mathbf{p}. \quad (2)$$

Following theoretical considerations [30,31], a fieldlike torque term was not taken into account in Eq. (2) due to the condition $d \gg \lambda_{\text{STT}}$. Further experimental support can be obtained from Fig. 4(b) in Ref. [8], where the P-MOKE signal proportional to m_z responds to the STT stimulus with a significant delay. On the contrary, the L-MOKE response immediately follows the spin current-driven accumulation of magnetic moment in Fe, corroborating the dominant role of the damping-like torque term in the STT-induced spin dynamics. If a fieldlike torque term would be active, the P-MOKE signal should respond to the spin current excitation directly.

The reported in-plane excursion of the magnetization of $m_y = \frac{M_y}{M_0} = 0.023$ directly after the spin current pulse arrival allows us to determine the respective current density to be used in the simulations. For this purpose, we systematically varied the current density and analyzed the temporal evolution of the in-plane component m_y . The maximum excursion appears shortly after the spin current pulse maximum, which is in agreement with Ref. [8] [see Fig. 4(b) therein]. Figure 2 shows that the maximum depends linearly on the applied current density. The linear interpolation intersects with the horizontal dashed line defined by the experimental value of m_y at $j_0 = 5.9 \times 10^{12} \text{ A/m}^2$. This result in an excellent agreement with the one obtained from the spin-transfer density ($7\mu_B/\text{nm}^2$) evaluated in Ref. [8] ($\approx 6 \times 10^{12} \text{ A/m}^2$), thus reinforcing our micromagnetic model. Further, this j_0 value is realistic, as it corresponds to the $\sim 10\%$ spin transport-induced demagnetization of a 10-nm-thick Fe film within 200 fs, in agreement with the latest results obtained within the superdiffusive transport model [23]. Moreover, it is close to the values reported in other works (10^{12} – 10^{13} A/m^2 , Ref. [32], and 10^{13} A/m^2 , Ref. [33]). Similar numbers can be further obtained from the work of Choi *et al.* [34] ($\sim 10^{12} \text{ A/m}^2$).

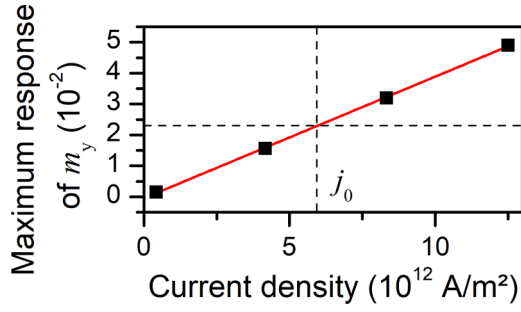


FIG. 2. Determination of the charge current density j_0 carrying the spin current [see prefactor in Eq. (1)] from the simulated dependence of the maximum of m_y on j_0 (closed rectangles). The continuous line is a linear fit to these data. The horizontal dashed line marks the experimentally found maximum of $m_y = 0.023$ [8], which corresponds to $j_0 = 5.9 \times 10^{12}$ A/m² (see vertical dashed line).

III. RESULTS

A. Coherent magnon generation

In the first numerical experiment, conducted at temperature $T = 0$, we prepared a spin current pulse with polarization $\mathbf{p} \parallel$

$\mathbf{y} \perp \mathbf{m}$. Then, according to Eq. (2), the spin torque will be $\tau_{\text{STT}} \perp \mathbf{m}$. The subsequent spatially resolved spin dynamics was computed for a total time of 1 ns after the spin current pulse peak. Figure 3(a) shows m_i^{dyn} , which is the dynamic part of the laterally averaged magnetization component $\langle m_i \rangle_{x,y}(z, t)$ ($i = x, y, z$) in each layer of the Fe film for the first 8 ps. In particular, we define $m_x^{\text{dyn}} = \langle m_x \rangle_{x,y} - 1$, $m_y^{\text{dyn}} = \langle m_y \rangle_{x,y}$, and $m_z^{\text{dyn}} = \langle m_z \rangle_{x,y}$. See also movie 1 in Ref. [35] for an animated version of the data. One can see how the spin current induces the formation of a localized wave packet which then expands. Note that the quadratic dispersion of exchange-dominated spin waves [36]

$$f(k) = \frac{\gamma \mu_0}{2\pi} \sqrt{\left(H_{\text{an}} + \frac{2A_{\text{ex}}}{M_0} k^2\right) \left(H_{\text{an}} + \frac{2A_{\text{ex}}}{M_0} k^2 + M_0\right)} \quad (3)$$

is responsible for the quick spatial broadening of the spin-wave packet. Here, $\frac{\gamma}{2\pi} \approx 28$ GHz/T is the gyromagnetic ratio, $H_{\text{an}} = 2K_u/M_0$ is the in-plane crystalline anisotropy field, A_{ex} the exchange constant, M_0 the saturation magnetization, and $\mu_0 = 4\pi \times 10^{-7}$ N/A² the magnetic permeability of vacuum.

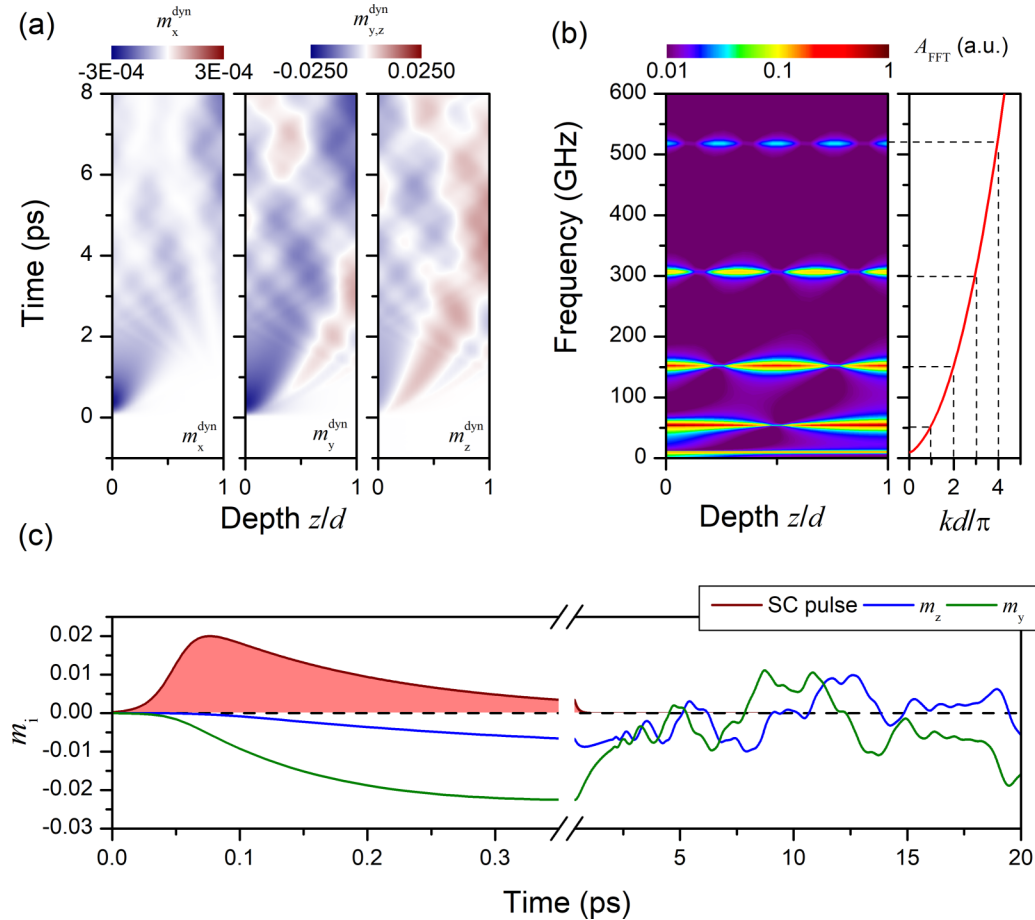


FIG. 3. Magnetization dynamics driven by the ultrafast spin-transfer torque. (a) Spatiotemporal plot of the dynamic part $\langle m_i^{\text{dyn}} \rangle$ of laterally averaged dynamic magnetization components. The left panel of (b) shows a spatially resolved, temporal Fourier transform of the $\langle m_z \rangle$ data shown in the right panel of (a), and the right panel of (b) shows the spin-wave dispersion $f(k)$ from Eq. (3). The dashed lines relate the numerical response to the analytic theory. (c) Simulated ultrafast dynamics of m_y and m_z projections at the Au/Fe interface. The red shaded area represents the spin current pulse profile according to Eq. (1).

The front of the spin-wave packet in Fe (not to confuse with the wavefront of the spin current pulse formed by hot spin-polarized electrons which propagate in Au with the Fermi velocity) travels with a characteristic speed of about 7 nm/ps. This value corresponds to the group velocity of the magnons with the largest wave vectors contained in the excitation spectrum. After about 2 ps, the wave packet has reached the surface of the Fe film. The spin dynamics for times $t > 2$ ps is formed by an interference pattern, which can be well analyzed by a Fourier transformation in time, as shown in Fig. 3(b). There, the local Fourier amplitude

$$A_{\text{FFT}}\{\langle m_z \rangle_{x,y}\}(z, f) = \left| \sum_{j=0}^{N-1} \langle m_z \rangle_{x,y}(z, t_j) e^{-i2\pi f t_j} \right| \quad (4)$$

is depicted, with frequencies $f = 0, \frac{1}{t_{\text{max}}}, \dots, \frac{N}{t_{\text{max}}}$. The subscript FFT indicates that we utilize a numerical fast Fourier transform algorithm (FFTW3), which we apply locally (z -resolved) to the laterally averaged, out-of-plane magnetization component $\langle m_z \rangle_{x,y}$. The temporal sampling goes from time $t = 0$ up to $t_N = t_{\text{max}} = 1$ ns, in equidistant steps of 10 fs.

In agreement with the experiment [8], this representation reveals that the pattern from Fig. 3(a) can be understood as a superposition of standing spin waves. This is emphasized by the right panel in Fig. 3(b), which shows the dispersion (3), plotted as a function of a dimensionless wave number $\kappa = kd/\pi$. Prominent spin dynamics can be found at integer $\kappa_n = k_n d/\pi = 0, 1, 2, \dots$, and the corresponding eigenmode frequencies $f_n = f(\kappa_n)$.

Having established the agreement between the results of micromagnetic simulations and the experimental data in the quasiequilibrium (nanosecond) regime, we now turn to much faster timescales. Taking advantage of the subnanometer spatial resolution along the out-of-plane direction in the Fe film, in Fig. 3(c), we plot the evolution of the magnetic moment at the Au/Fe interface, i.e., where the spin current pulse is injected. In contrast to the experimental MOKE data, which are given by the convolution of a magnetization profile and MOKE sensitivity functions [37], these data allow for a deeper insight into the spin-wave dynamics. First, we turn to the subpicosecond timescale (the left-hand side) where the spin-wave propagation has not played a significant role yet. It is seen that the in-plane projection of the magnetic moment m_y quickly grows as a result of the spin injection, whereas the dynamics of the out-of-plane component m_z is delayed. Similar behavior found in the experimental data (cf. Fig. 4(b) in Ref. [8]) corroborates our understanding of the spin injection picture on the ultrafast timescale.

Later on, the magnetization dynamics at the interface represents a compendium of oscillations corresponding to the individual spin waves, see Fig. 3(c), the right-hand part. A close inspection reveals the excitation of up to nine spin-wave eigenmodes of the 14.2-nm-thick Fe film, thus exceeding the experimental reports. However, we emphasize that the aforementioned intrinsic spatial averaging of the MOKE signals precludes the observation of extremely short-wavelength modes. In that regard, the data in Fig. 3 illustrate that the qualitative agreement between the simulations and the experiment holds on femtosecond through nanosecond timescales. As such, it

is reasonable to use the predictions of the micromagnetic approach to model the picosecond spin dynamics as well. We note, however, that aiming at the quantitative agreement with the experimental data in the presence of nonequilibrium magnons would require more sophisticated modeling of the measurement process and measured quantities, as well as refined description of the spin current pulse injection. Furthermore, such comparisons would strongly benefit from experimental probing methods with better spatial resolution, as compared to MOKE.

Besides reproducing experimental findings, the micromagnetic model allows for an identification of the parameters that govern the mode-specific excitation efficiency. As such, we will now discuss the energy transfer into the different spin-wave modes. For this purpose, we analyze in detail squared FFT amplitude spectra at the interface of the Fe film, $z = 0$. This choice is motivated by the first order boundary conditions for the spin-wave modes ensuring the largest amplitude of the oscillations of the spin projections at the interfaces of the Fe film [36]. The integration of the $A_{\text{FFT}}^2(f)$ spectrum in the vicinity of the peaks corresponding to the excitation of the different spin-wave modes yields the partial energies ε_n associated with each of the modes:

$$\varepsilon_n = \int_{f_n - \Delta f}^{f_n + \Delta f} A_{\text{FFT}}^2(f) df. \quad (5)$$

This quantity is proportional to the energy transferred into this mode. In what follows, we shall focus on various factors that contribute to ε_n , aiming at understanding their importance for a comparative analysis of the excitation efficiency of the PSSW modes in thin ferromagnetic films. In Appendix, we develop an analytic formalism based on the Holstein-Primakoff transformations, which is capable of deriving the contributing factors in detail [see Eqs. (A1) to (A15)]. Importantly, the energy supplied by a spin current pulse $j_s(z, t)$ is proportional to the product of spatial Fourier power,

$$|\tilde{\beta}|^2(\mathbf{k}_n) = \beta(\mathbf{k}_n)\beta^*(\mathbf{k}_n), \quad (6)$$

and the temporal Fourier power

$$|\tilde{\theta}|^2(\omega_n) = \tilde{\theta}(\omega_n)\tilde{\theta}^*(\omega_n) \quad (7)$$

of the spin current $j_s(z, t)$ defined by Eq. (1), evaluated at $k = k_n$ and $\omega = \omega_n$. Note that in the appendix, we use analytic formulas. In particular there, we thus refer to

$$\beta(\mathbf{k}_n) = \frac{\gamma \hbar j_0}{2e\mu_0 M_0 2\pi} \int_0^d dz e^{-z/\lambda_{\text{STT}} - i n \pi z/d} \quad (8)$$

and

$$\tilde{\theta}(\omega_n) = \frac{1}{2\pi} \int_{-\infty}^{\infty} dt \frac{e^{-t/\tau_2}}{1 + e^{-(t-t_0)/\tau_1}} e^{-i\omega_n t}, \quad (9)$$

where $\omega_n = 2\pi f_n$. In contrast, to numerically evaluate the two factors $|\tilde{\beta}|^2(\mathbf{k}_n)$ and $|\tilde{\theta}|^2(\omega_n)$, and also to compute the partial powers ε_n , we use discrete fast Fourier transform algorithms. To avoid having to unify different prefactor conventions, we will from now on disregard all irrelevant prefactors, and only discuss proportionalities.

The two factors $|\tilde{\beta}|^2(\mathbf{k}_n)$ and $|\tilde{\theta}|^2(\omega_n)$ are shown as a function of the mode index n in Fig. 4(a) for $\lambda_{\text{STT}} = 2$ nm.

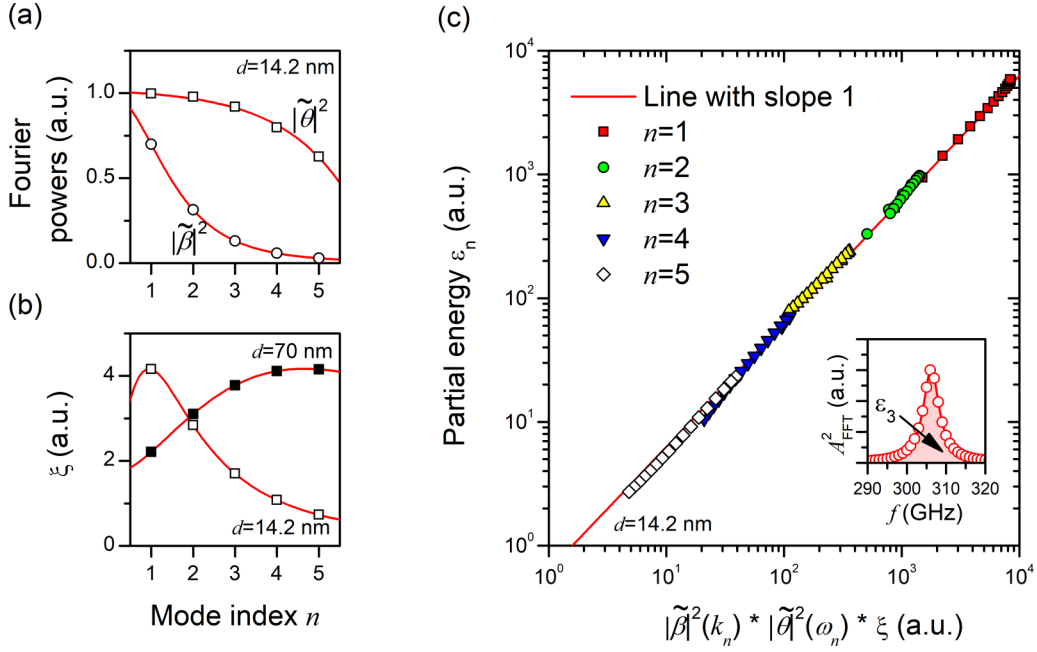


FIG. 4. PSSW excitation efficiency. (a) Squared spatial $|\tilde{\beta}|^2$ and temporal $|\tilde{\theta}|^2$ Fourier amplitudes of the spin-current pulse (1) as a function of the PSSW mode index for $d = 14.2$ nm and $\lambda_{\text{STT}} = 2$ nm. The lines are shown as a guide to the eye. (b) Additional ξ factor as a function of the PSSW mode index for two different Fe film thicknesses d (14.2 nm, open squares, and 70 nm, full squares). (c) Correlationlike double logarithmic plot of the partial energy ε_n vs the product of the various factors, which govern the energy transfer, $|\tilde{\beta}|^2 |\tilde{\theta}|^2 \xi$. The different colors indicate various PSSW eigenmodes while within a single color, the data points are obtained for different values of λ_{STT} . The solid line is a linear fit to the data.

Note that the temporal factor $|\tilde{\theta}|^2$ is only important when the oscillation period $T_n = 1/f_n$ approaches the duration of the spin current stimulus $\sim \tau_2$. Thus, in our case for $n < 5$ and ~ 250 fs spin current pulse duration, the spatial factor $|\tilde{\beta}|^2$ plays a dominant role in determining the relative excitation efficiency of the PSSW modes.

Further, we identify in Appendix the material parameter-dependent susceptibility of the different spin-wave modes, which, together with their ellipticity \mathcal{E}_k , gives rise to another factor $\xi = \frac{\Gamma_k}{\omega_k} \frac{1-\mathcal{E}_k}{2-\mathcal{E}_k}$. Figure 4(b) shows the dependence of ξ on the mode number n for two different film thicknesses. For thin films exemplified here as $d = 14.2$ nm, the ξ factor peaks at $n = 1$ and further decays for higher modes. As this dependence is similar to the behavior of β_{k_n} , the role of ξ for the relative excitation efficiency consists in emphasizing the mode with $n = 1$, consistent with the experimental data [8]. However, for thicker films, the maximum of ξ is shifted towards higher modes ($n = 5$ for $d = 70$ nm). Note that because in those films both ω and k only slightly increase with n , for small n (when $k_n \lambda_{\text{STT}} \ll 1$, $\omega_n \tau_2 \ll 1$) the other factors $|\tilde{\beta}|^2(\mathbf{k}_n)$ and $|\tilde{\theta}|^2(\omega_n)$ are both almost constant. As such, up to much larger n , the dynamical response is dominated by ξ and thus can be enhanced at higher ($n > 1$) order spin-wave modes. Supported by the analytic theory, we expect in summary a linear relation

$$\varepsilon_n \propto |\tilde{\beta}|^2(\mathbf{k}_n) |\tilde{\theta}|^2(\omega_n) \xi. \quad (10)$$

Indeed, Fig. 4(c) shows that a linear scaling law holds over four decades. The data shown here were obtained by varying λ_{STT} between 0.5 and 5 nm. The excellent agreement between the predictions of the analytic calculations and the results of

numerical simulations emphasizes that all significant factors are accounted for in Eq. (10).

Having outlined the factors contributing to the excitation efficiency of the PSSW modes in thin films, we can now build a bridge to the experiment. We note that in Ref. [8] an upper boundary for λ_{STT} has been identified, based on the spin current pulse ability to excite the spin-wave mode with $n = 4$. Here, the above mentioned formalism enables the determination of a *lower* λ_{STT} boundary. The critical conditions for that rely on the fact that the excitation efficiency for $n = 5$ mode was found insufficient for its unambiguous detection in the experimental data. Clearly, for smaller λ_{STT} , the $n = 5$ mode will be more strongly excited. As such, we can calculate the ratio

$$r_{15} = s_{15} A_1 / A_5 \quad (11)$$

for various λ_{STT} , where A_n is the Fourier amplitude of the n th PSSW mode at the interface. The correction factor s_{15} takes into account that in the experiment the MOKE in-depth sensitivity function $w(z)$ is responsible for the fact that different PSSW modes contribute unequally to the total MOKE signal. We calculate $w(z)$ using an optical transfer matrix method [37], and determine s_{15} , in order to enable direct comparison with the experimental peak-to-noise ratio $r_{\text{exp}} = \frac{A_1^{\text{exp}}}{A_N}$, where A_N is the experimental noise level. We arrive at the following condition for λ_{STT} :

$$r_{15}(\lambda_{\text{STT}}) \geq \frac{A_1^{\text{exp}}}{A_N}. \quad (12)$$

In Fig. 5, we show the dependence of the peak ratios on λ_{STT} . The intersection of the red (experimental) and black

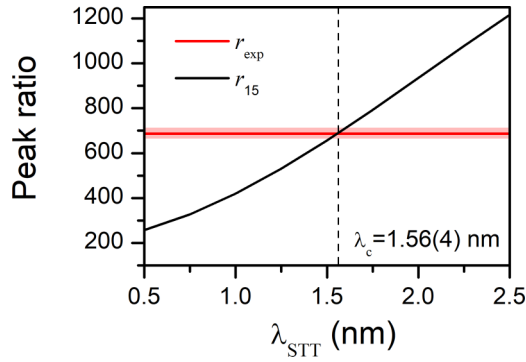


FIG. 5. Determination of a lower boundary for the spin-transfer torque characteristic depth λ_{STT} . Simulated (black) peak ratio of the amplitudes of the first and fifth spin-wave eigenmodes r_{15} [Eq. (11)] as a function of λ_{STT} . The red horizontal line indicates the signal-to-noise level in the experiments [8], the red shaded region indicates the corresponding error bar. The vertical dashed line shows the estimated lower boundary λ_c .

(simulated) curves indicates the lower boundary for λ_{STT} of about 1.56 nm.

B. Incoherent magnon creation and annihilation

As a second numerical experiment, we prepared a spin current pulse whose polarization \mathbf{p} is collinear to \mathbf{x} , and thus to the Fe magnetization \mathbf{m} . Then, according to Eq. (2) at temperature $T = 0$ the spin torque τ_{STT} vanishes, and no coherent spin dynamics can be expected. At finite temperatures this expectation is, however, misleading due to the magnetic fluctuations present in the ferromagnet. Practically, these fluctuations manifest as a reduction of the average magnetization. Averaging in time gives the transverse components $\langle m_{y,z} \rangle_t = 0$, and the longitudinal component $\langle m_x \rangle_t < 1$. The larger the temperature, the smaller is the longitudinal magnetization component. Switching on a spin current pulse with \mathbf{p} collinear to \mathbf{x} acts only on the transverse components, which are momentarily nonzero. It is well known from conventional magnonics, that the resulting torque is damping- or antidamping-like, and that thermal fluctuation will therefore be suppressed or enhanced [24]. This sort of magnon cooling or heating should also manifest on ultrafast time scales in either an increase, or a further decrease of the longitudinal magnetization component.

In the following, we will discuss simulation results obtained for $\lambda_{\text{STT}} = 2$ nm at $T = 100, 200$, and 300 K. Note that before the spin current pulse is injected, we determined a thermal average by first increasing the temperature to the desired value, and then letting the system evolve for 5 ns. This value was found sufficient to ensure that the system reaches the equilibrium and does not evolve further. In Fig. 6(a), we plot the temporal form of the spin current pulse according to Eq. (1). In Fig. 6(b), we show the temporal evolution of the spatially averaged longitudinal magnetization component $\langle m_x \rangle_{xyz}$ for $T = 100$ K. See also movie 2 in Ref. [35] for an animated version of the data. When the spin current pulse penetrates into the film, the fluctuations increase (decrease), in case of $\mathbf{p} \parallel \mathbf{x}$ ($\mathbf{p} \perp \mathbf{x}$). Therefore simultaneously the longitudinal magnetization component further decreases (increases). Note

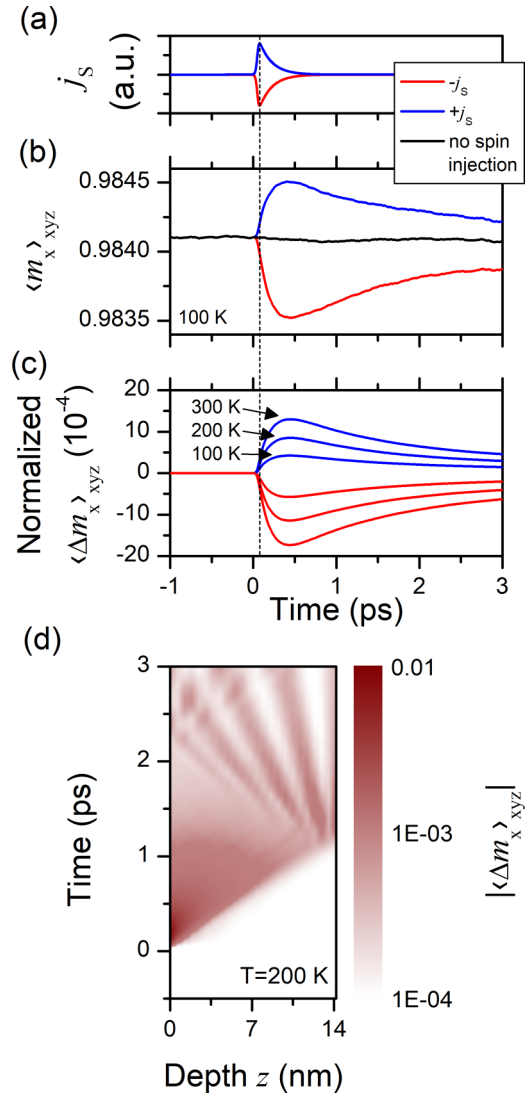


FIG. 6. Suppression and enhancement of incoherent magnon dynamics by spin currents. (a) Temporal shape of the spin-current pulse $j_s(t)$ of the two opposite polarities. (b) Simulated time dependence of the spatially averaged longitudinal magnetization component $\langle m_x \rangle$ at $T = 100$ K. (c) Variations of spatially averaged longitudinal magnetization component $\langle m_x \rangle$, normalized to that obtained in the case of no spin current injection. Multiple lines show the results calculated for three various temperatures, as indicated by dark arrows. The dashed line in (a) through (c) indicates the peak time of the spin current pulse. (d) Layer-resolved, only laterally averaged, normalized change of the longitudinal magnetization component $\langle m_x \rangle$ obtained at the temperature of 200 K.

that we only show single time series in Fig. 6(b). The deterministic nature of the thermal noise in the numerical simulation enables us to apply a normalization procedure to the case when no spins are injected into the ferromagnet. Normalizing and shifting yields the quantity $\langle \Delta m_x \rangle_{xyz} = \frac{\langle m_x \rangle_{xyz}(j_s \neq 0)}{\langle m_x \rangle_{xyz}(j_s = 0)} - 1$, which is shown in Fig. 6(c). This representation clearly shows that the maximum of the change in the magnetic moment is shifted by 360 fs with respect to the maximum of the spin current, marked by the vertical dashed line. It can be shown that the front of the transient normalized $\langle \Delta m_x \rangle_{xyz}$ can

be approximated with the time-integrated spin current pulse profile, indicating the accumulative nature of the effect. At later times, both signals decay approximately exponentially with a time constant of $1.79(1)$ ps. Since in our modeling (both numerical and analytical, see Appendix) this decay originates in Gilbert damping only, one can deduce that the spin-wave modes with frequencies of a few THz dominate the dynamic response.

We note that the change of the longitudinal moment is with only 10^{-3} rather small. As a matter of fact, it increases proportional to the temperature, as Fig. 6(c) shows. Recall that so far we were discussing spatial averages. By applying the normalization procedure to each layer of the simulated film, we have obtained the spatially resolved data shown in Fig. 6(d). There one can see that at the injection side the change increases by one order of magnitude, compared to the averaged dynamics. Note that Fig. 6(d) looks qualitatively similar to the left panel in Fig. 3(a). However, in contrast to the data shown there, here the spin injection does not cause spatiotemporal coherence of the spin dynamics. Instead, the data plotted in Fig. 6(d) should be interpreted as a spatiotemporal modulation of the density of thermal magnons in the film.

IV. OUTLOOK: OPTICAL SPIN-WAVE EXCITATION BEYOND THE DIFFRACTION LIMIT

So far, we have been discussing the spin-wave (magnon) eigenmodes which are quantized in the direction perpendicular to the film. When considering optical excitation of laterally propagating magnons, one has to acknowledge that this process is usually limited by diffraction. As already mentioned in the introduction, this implies that optical excitation of magnons with wavelengths below the light wavelength is rather inefficient. We will now show that spin currents offer a unique possibility to overcome this limitation. Consider a multilayer as in Ref. [8], but with the top Fe layer patterned into stripes, as depicted in Fig. 7(a). There, the spin current generation, and subsequently the magnon generation in the bottom Fe layer is governed by the geometry of the stripes instead of the laser spot size. To model this situation, we again employed the spatiotemporal shape of the spin current pulse given by Eq. (1). In addition, a lateral mask defined by six stripes (width $w = 10$ nm and spatial period $s = 20$ nm) was imposed to model the structure shown in Fig. 7(a). As such, the lateral cross-section of the laser-generated spin current pulse reproduces the mask stripe pattern. We used $8192 \times 1 \times 10$ cells of size 0.5^3 nm³, which were enlarged again into a film by applying periodic boundary conditions in x and y direction.

In Fig. 7(b), we show a map of the transient magnetization component $\langle m_z \rangle_{a,yz}(x, t)$, averaged across y , z , and across a width of $a = 2$ nm around equidistantly probed locations at a distance x towards the center of the stripes. The data clearly show the lateral emission of a spin-wave packet, moving with a velocity of about 2500 ± 200 m/s. A Fourier transformation in time and space reveals the spectral properties of the spin dynamics, as shown in Fig. 7(c). Here, one can see that the dispersion $f(k)$ of dipole-exchange spin-waves in Fe [36] [see the dashed line in Fig. 7(c)] falls on top of the regions of strong response in the spectrum. Reflecting the periodicity of the stripe pattern, the strongest response can be seen around

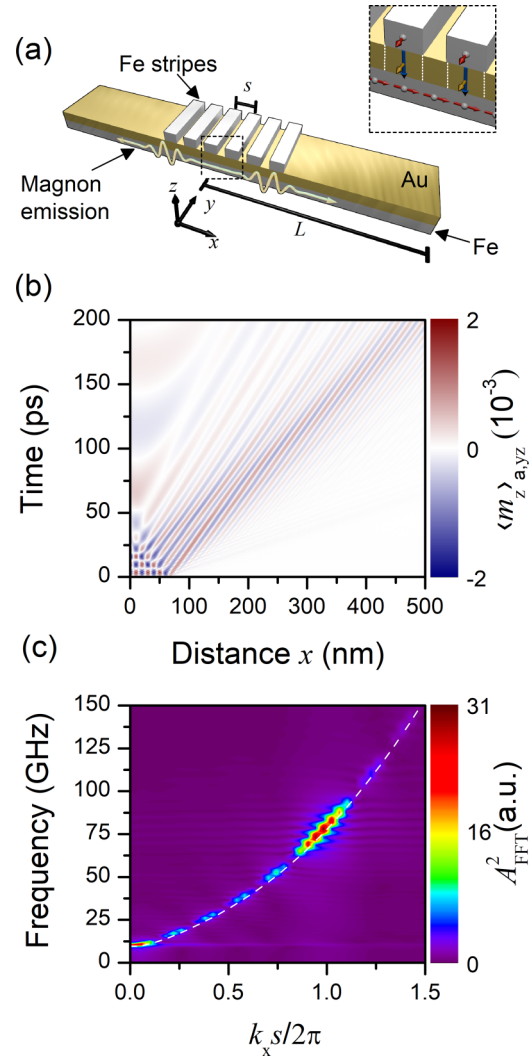


FIG. 7. Excitation of the in-plane propagating spin waves. (a) Conceptual device design. Femtosecond laser pulse excites the periodically striped top Fe layer, resulting in generation of a spatially modulated spin current pulse. The latter reaches the underlying orthogonally magnetized Fe layer. The resulted spin-transfer torque excites propagating spin waves. Magnifying the active area, the inset shows the spin orientations in the Fe layers, and the spin current flow in the nonmagnetic spacer. The stripe period is denoted with s , while $L = 500$ nm is the maximum probing length. (b) Spatiotemporal plot of the averaged out-of-plane magnetization component $\langle m_z \rangle_{a,yz}(x, t)$. (c) Two-dimensional Fourier transform of the data shown in (b), indicating efficient excitation of spin waves with wave numbers governed by the stripes periodicity s , i.e., at $k = 2\pi/s$. The white dashed line shows the dispersion of dipole-exchange spin waves according to Ref. [36].

$f = 75$ GHz and $k_x = 2\pi/s$. The group velocity at this wave number $v_g = \frac{\partial \omega}{\partial k}(2\pi/s) \approx 2600$ m/s is in a good agreement with the propagation speed of the spin-wave packet in Fig. 7(b).

V. CONCLUSIONS

In summary, we have shown that the action of ultrafast spin currents penetrating into a magnetic thin film can be modeled in great agreement with experimentally found

ultrafast response and the spectral properties of the subsequent magnetization dynamics between 10 and 500 GHz by including a Slonczewski-like spin-torque term in the micromagnetic equation of motion. Note that, so far, experimental limitations inhibit the detection of spin-wave modes with frequencies above ~ 1 THz [9]. In principle, an optical experiment similar to Refs. [8,9] can be conceived, where smaller thicknesses of the collector Fe film would effectively shift the frequencies of the spin-wave modes up into the THz range. If, in addition, probe light with much shorter wavelength, and thus shorter penetration depth would be used, this would enable the observation of high-frequency spin-wave modes and comparisons with the predictions of our model.

In this work, we have shown that depending on the polarization of the spin current, the resulting torque can either create or annihilate coherent or incoherent magnons. In particular, we reproduced the recent experimental demonstration of coherent magnon generation by spin currents, and obtained further insights into the spatial scales involved in this process. We have identified the factors contributing to the relative excitation efficiency and shown that the linear proportionality law holds over four orders of magnitude. Lastly, employing numerical simulations, we complemented the experimentally estimated constraints on the characteristic spin-transfer torque depth λ_{STT} in Fe.

Further, our analysis of the spin current excitation of incoherent magnons indicates that the simulated ultrafast heating and cooling should be detectable by magneto-optical methods. We note here that the heating effects which are not explicitly accounted for in our model might introduce additional complications. Both thermal and spin current-driven signals will be overlaid in time, but can in principle be distinguished by their symmetry properties. Considering thinner ferromagnetic films and larger densities of the injected spin current, as in Ref. [38], our modeling suggests that the hot electrons-driven spin-transfer torque can be a relevant and viable ansatz to understand the observed spin dynamics. We nevertheless acknowledge that under more extreme conditions a transient change of the magnetization itself, and increased thermal fluctuations cannot be neglected in order to obtain a complete picture. Then, more elaborate modeling techniques such as those described in Refs. [26,39] are needed.

In the outlook section, we discussed a way to overcome the diffraction limit when exciting propagating in-plane spin waves. The basic idea relies on the fact in Fe/Au/Fe trilayer spin valve trilayers [8,28], nanostructuring of the top, laser-excited layer enables spatial tailoring of the spin current profile. In the simplest case, spin currents can only be excited where the top Fe layer exists, thus introducing an in-plane inhomogeneity into the STT stimulus. We have shown that geometrical patterning enables the excitation of propagating spin waves with wavelengths considerably smaller than the optical diffraction limit of typically used VIS to NIR-VIS laser sources. Note that the proposed device design lifts the restriction pertinent to the use of epitaxial Fe films for setting up their magnetizations directions. Indeed, the latter can be achieved exploiting the shape anisotropy of the stripes, and an external magnetic field can be used to ensure an orthogonal magnetization in the bottom Fe layer, instead of relying on magneto-crystalline anisotropy. As such, spin current-driven excitation of high-frequency spin

waves in amorphous ferromagnets (e.g., low-loss CoFeB) or even insulating materials (such as yttrium iron garnet attracting increased attention recently) remains an intriguing perspective.

To conclude, we emphasize that this work shows that experimental observations from conventional magnonics and recent ultrafast experiments can be explained on equal theoretical footings. We are convinced that our findings open a fruitful perspective for the application of the predictive and interpretative power of micromagnetic simulation in experimental ultrafast magnetism.

ACKNOWLEDGMENTS

H.U. acknowledges financial support by the Deutsche Forschungsgemeinschaft within project A06 of the SFB 1073 “Atomic scale control of energy conversion.” The authors thank A. Melnikov and C. Seick for valuable comments and M. Wolf for continuous support.

APPENDIX: A CLASSICAL HAMILTONIAN VIEW

The theoretical concepts for the following description were first outlined by H. Suhl [40] and V.S. L’vov [41]. This theory can be regarded as analytic micromagnetic modeling. Note that it has been successfully employed to describe spin-current driven magnetization dynamics in conventional magnonic studies [42–45]. Consider a thin ferromagnetic film of thickness $d = 14.2$ nm, supporting magnons with amplitudes $b_{\mathbf{k}}$, frequencies $\omega_{\mathbf{k}}$, and relaxation rates $\Gamma_{\mathbf{k}}$. According to Suhl, the magnetization dynamics, as described by the Landau-Lifshitz (LL) equation

$$\dot{\mathbf{M}} = -\gamma\mu_0\mathbf{M} \times \mathbf{H}_{\text{eff}} \quad (\text{A1})$$

can be analyzed into plane spin waves, and the dynamics of these modes can be described by simple kinetic equations. The first step is to linearize the LL equation (A1), and then apply the first Holstein-Primakoff transformation (HPT) to calculate

$$\dot{m}^+ = \sum_{\mathbf{k}} \dot{a}_{\mathbf{k}} e^{i\mathbf{k}\mathbf{r}} = \dot{m}_y + i\dot{m}_z, \quad (\text{A2})$$

where $m_i = M_i/M_0$. The second HPT takes into account ellipticity of the precession in a tangentially magnetized film. It finally maps $a_{\mathbf{k}}$ to the amplitudes $b_{\mathbf{k}}$. In total, the HPTs diagonalize the Hamiltonian \mathcal{H} , which generates the LL equation (A1). Without dissipation and interactions, \mathcal{H} then simply reads

$$\mathcal{H} = \sum_{\mathbf{k}} \hbar\omega_{\mathbf{k}} b_{\mathbf{k}} b_{\mathbf{k}}^*. \quad (\text{A3})$$

Note that for the dispersion $\omega_{\mathbf{k}} = \omega(\mathbf{k})$ we take the approximation Eq. (3) in the main text. The canonical equation of motion for the spin-wave amplitudes is then

$$\dot{b}_{\mathbf{k}} + i\omega_{\mathbf{k}} b_{\mathbf{k}} = 0. \quad (\text{A4})$$

Adding a Gilbert-like dissipation term to the Eq. (A1), one gets

$$\dot{b}_{\mathbf{k}} + [i\omega_{\mathbf{k}} + \Gamma_{\mathbf{k}}] b_{\mathbf{k}} = 0, \quad (\text{A5})$$

where the relaxation rate is given by

$$\Gamma_{\mathbf{k}} = \alpha\omega_H \frac{\partial\omega}{\partial\omega_H}, \quad (\text{A6})$$

with $\omega_H = \gamma\mu_0 H + \gamma\mu_0 \frac{2A_{\text{ex}}}{M_0} k^2$.

a. Coherent magnon generation

For the case of our spatially inhomogeneous spin current, similar to Ref. [42], we first introduce the quantity

$$\beta(t, \mathbf{r}) = \frac{\gamma \hbar j_0}{2e\mu_0 M_0} e^{-z/\lambda_{\text{STT}}} \frac{e^{-t/\tau_2}}{1 + e^{-(t-t_0)/\tau_1}}. \quad (\text{A7})$$

It is then convenient to consider a Fourier representation of β , and separate out the time-dependence:

$$\beta(t, \mathbf{r}) = \theta(t) \sum_{\mathbf{k}} \beta_{\mathbf{k}} e^{i\mathbf{k}\mathbf{r}}. \quad (\text{A8})$$

If $\mathbf{p} \perp \mathbf{M}$, linearizing the STT term [Eq. (2)] results for the first HPT in

$$\dot{m}^+ = \dot{m}_y + i\dot{m}_z - \theta(t) \sum_{\mathbf{k}} \beta_{\mathbf{k}} e^{i\mathbf{k}\mathbf{r}}. \quad (\text{A9})$$

The rate equation for a particular mode amplitude $b_{\mathbf{k}}$ then reads

$$\dot{b}_{\mathbf{k}} + [i\omega_{\mathbf{k}} + \Gamma_{\mathbf{k}}]b_{\mathbf{k}} - \theta(t)\beta_{\mathbf{k}} = 0. \quad (\text{A10})$$

On short timescales $t \ll \frac{1}{\Gamma_{\mathbf{k}}}, \frac{2\pi}{\omega_{\mathbf{k}}}$, the second term in Eq. (A10) can be neglected. Direct integration yields, if the initial dynamic amplitude is small:

$$b_{\mathbf{k}}(t) = \beta_{\mathbf{k}} \int_0^t \theta(t') dt'. \quad (\text{A11})$$

Summation over the all \mathbf{k} modes and Fourier transformation back into real space gives

$$m_y(t, z) = \beta(z) \int_0^t \theta(t') dt', \quad (\text{A12})$$

whereas $m_z(t, z) = 0$. This result implies that one can obtain the temporal shape of the spin current pulse $\theta(t)$ by taking the time derivative of $m_y(t)$ probed in the corresponding MOKE geometry (e.g., by L-MOKE in Fig. 4(b) from Ref. [8]). Furthermore, here it is seen why we call this process coherent. In a stroboscopic pump-probe experiment, one always induces deterministic growth of a transverse magnetization component with the same phase.

For longer time scales, one needs to consider all terms in Eq. (A10). Note that a constant spin current $\theta(t) = \theta_0$ leads to a new equilibrium orientation of the magnetization, whereas a time-limited spin current pulse $\theta(t)$ pumps energy into the different spin-wave modes. Here we assume that the perturbation is small so that the orientation of the magnetization remains unchanged. Applying a time-domain Fourier transformation to Eq. (A10) and its complex conjugate, we get

$$\begin{aligned} i\omega \tilde{b}_{\mathbf{k}} + [i\omega_{\mathbf{k}} + \Gamma_{\mathbf{k}}]\tilde{b}_{\mathbf{k}} - \tilde{\theta}(\omega)\beta_{\mathbf{k}} &= 0, \\ i\omega \tilde{b}_{\mathbf{k}}^* + [-i\omega_{\mathbf{k}} + \Gamma_{\mathbf{k}}]\tilde{b}_{\mathbf{k}}^* - \tilde{\theta}^*(\omega)\beta_{\mathbf{k}}^* &= 0. \end{aligned} \quad (\text{A13})$$

Thus the power spectrum of a given mode \mathbf{k} reads

$$p_{\mathbf{k}}(\omega) = \tilde{b}_{\mathbf{k}} \tilde{b}_{\mathbf{k}}^* = \frac{\tilde{\theta}(\omega) \tilde{\theta}^*(\omega) \beta_{\mathbf{k}} \beta_{\mathbf{k}}^*}{\omega_{\mathbf{k}}^2 - \omega^2 + \Gamma_{\mathbf{k}}^2 + 2i\omega\Gamma_{\mathbf{k}}}. \quad (\text{A14})$$

To obtain the absorbed partial energy $\varepsilon_{\mathbf{k}}$ introduced in Eq. (5), we integrate $p_{\mathbf{k}}(\omega)$ over the frequency range:

$$\begin{aligned} \varepsilon_{\mathbf{k}} &\sim \text{Im} \left[\int_0^\infty p_{\mathbf{k}} d\omega \right] \\ &\approx \tilde{\theta}(\omega_{\mathbf{k}}) \tilde{\theta}^*(\omega_{\mathbf{k}}) \beta_{\mathbf{k}} \beta_{\mathbf{k}}^* \frac{\tan^{-1} \frac{\Gamma_{\mathbf{k}}}{\omega_{\mathbf{k}}}}{\omega_{\mathbf{k}}} \\ &\approx \tilde{\theta}(\omega_{\mathbf{k}}) \tilde{\theta}^*(\omega_{\mathbf{k}}) \beta_{\mathbf{k}} \beta_{\mathbf{k}}^* \frac{\Gamma_{\mathbf{k}}}{\omega_{\mathbf{k}}^2}. \end{aligned} \quad (\text{A15})$$

Here, we can already identify the factors $|\tilde{\theta}|^2(\omega) = \tilde{\theta}(\omega_{\mathbf{k}}) \tilde{\theta}^*(\omega_{\mathbf{k}})$, and $|\tilde{\beta}|^2(\mathbf{k}) = \beta_{\mathbf{k}} \beta_{\mathbf{k}}^*$ from Eq. (10). Confirming intuitive expectations, both spectral Fourier powers of the spatial and temporal factors directly impact the partial energy uptake of a particular spin current-driven spin-wave mode. Furthermore, we now explicitly derive the additional factor ξ , which appears crucial for the comparisons of the excitation efficiency between different modes. Recall that in the numerical simulation, we actually analyze the dynamics of the out-of-plane component m_z . When passing back from the amplitudes $b_{\mathbf{k}}$ to the magnetization, one has to take into account the ellipticity $\mathcal{E}_{\mathbf{k}}$ of the precession. We thus have to acknowledge that (see, e.g., Chap. 1 in Ref. [46])

$$\frac{|m_{\mathbf{k},z}|^2}{|m_{\mathbf{k},y}|^2} = 1 - \mathcal{E}_{\mathbf{k}}, \quad (\text{A16})$$

where

$$\mathcal{E}_{\mathbf{k}} = \left(1 + \frac{\gamma\mu_0 H + \gamma\mu_0 \frac{2A}{M_0} k^2}{\gamma\mu_0 M_0} \right)^{-1}. \quad (\text{A17})$$

When analyzing the partial energies of the modes found in the spectrum of m_z , the mode specific correction yields for the third factor in Eq. (5):

$$\xi = \frac{\Gamma_{\mathbf{k}}}{\omega_{\mathbf{k}}^2} \frac{1 - \mathcal{E}_{\mathbf{k}}}{2 - \mathcal{E}_{\mathbf{k}}}. \quad (\text{A18})$$

b. Incoherent magnon generation

We will now consider spin injection into a thermally occupied magnon ensemble. If we assume a spatially homogeneous spin current, whose polarization $\mathbf{p} \parallel \mathbf{M}$, the linearized contribution of the STT term to the LL equation (A1) results in

$$\dot{m}^+ = \dot{m}_y + i\dot{m}_z + \beta(t)m^+, \quad (\text{A19})$$

with the temporal dependence of β given by Eq. (2). The rate equation for $b_{\mathbf{k}}$ reads [42]

$$\dot{b}_{\mathbf{k}} + [i\omega_{\mathbf{k}} + \Gamma_{\mathbf{k}} + \beta(t)]b_{\mathbf{k}} = \mathcal{F}_{\mathbf{k}}, \quad (\text{A20})$$

where $\beta(t) = \gamma \frac{j_s(t)}{d\mu_0 M_0}$, and \mathcal{F} represents a thermal noise source. Note that in Eq. (A20) higher order terms in $b_{\mathbf{k}}$, which result from the second HPT, are not taken into account [42]. The product $\beta(t)b_{\mathbf{k}}$ in Eq. (A20) explains why the excitation process is incoherent. The random phase of a thermally driven magnon gets imprinted on the spin current term. Therefore, in a pump-probe experiment, the temporal evolution of the individual mode's phases will differ from shot to shot in a random fashion.

If the spin current is spatially inhomogeneous, one should again consider $\beta = \theta(t) \sum_{\mathbf{k}} \beta_{\mathbf{k}} e^{i\mathbf{k}\cdot\mathbf{r}}$. Then, in principle, different $\beta_{\mathbf{k}}$ induce a mixing between the magnon modes $b_{\mathbf{k}}$. The rate equation then reads

$$\dot{b}_{\mathbf{k}} + [i\omega_{\mathbf{k}} + \Gamma_{\mathbf{k}}]b_{\mathbf{k}} + \theta(t) \sum_{\mathbf{k}', \mathbf{k}''} \delta(\mathbf{k}' + \mathbf{k}'' - \mathbf{k}) \beta_{\mathbf{k}'} b_{\mathbf{k}''} = \mathcal{F}_{\mathbf{k}}. \quad (\text{A21})$$

For the experimental situation of a laterally homogeneous, but vertically inhomogeneous spin current, the mixing couples the modes with different k_z but equal k_x and k_y . To simulate the dynamics of a thermal magnon ensemble, we consider a volume of $v = dL^2$, and quantize the wave numbers according to $k_x = \frac{n\pi}{L}$, $k_y = \frac{m\pi}{L}$, $k_z = \frac{o\pi}{d}$, with $L = 10d$. Modes up to $m, n = \pm 256$ and $o = 24$ are taken into account. For the implementation of $\mathcal{F}_{\mathbf{k}}$, we have chosen a Gaussian random number generator, which obeys

$$\langle \mathcal{F}_{\mathbf{k}} \mathcal{F}_{\mathbf{k}'}^* \rangle = 2\delta(\mathbf{k} - \mathbf{k}') \Gamma_{\mathbf{k}} \frac{k_B T}{\hbar \omega_{\mathbf{k}}}. \quad (\text{A22})$$

In the absence of a spin current, this provides in the temporal average an equilibrium magnon number density of

$$|b_{\mathbf{k}}^{\text{eq}}|^2 = \langle b_{\mathbf{k}} b_{\mathbf{k}}^* \rangle = \frac{k_B T}{\hbar \omega_{\mathbf{k}}}. \quad (\text{A23})$$

To probe the dynamics, we determine the total number of magnons $\sum_{\mathbf{k}} b_{\mathbf{k}} b_{\mathbf{k}}^*$. Since each magnon carries $2\mu_B$, this reduces the magnetization to

$$m_x = \sqrt{1 - \frac{2\mu_B}{vM_s} \sum_{\mathbf{k}} b_{\mathbf{k}} b_{\mathbf{k}}^*}. \quad (\text{A24})$$

Similar to the analysis of the numerical simulations output, we then normalize the results by the equilibrium magnetization m_x^{eq} , defined by

$$m_x^{\text{eq}} = \sqrt{1 - \frac{2\mu_B}{vM_s} \sum_{\mathbf{k}} \frac{k_B T}{\hbar \omega_{\mathbf{k}}}}, \quad (\text{A25})$$

and shift by 1 to obtain

$$\Delta m_x = \frac{m_x}{m_x^{\text{eq}}} - 1. \quad (\text{A26})$$

Note that for comparing this analytic model with the micromagnetic model, we neglect the cross coupling terms

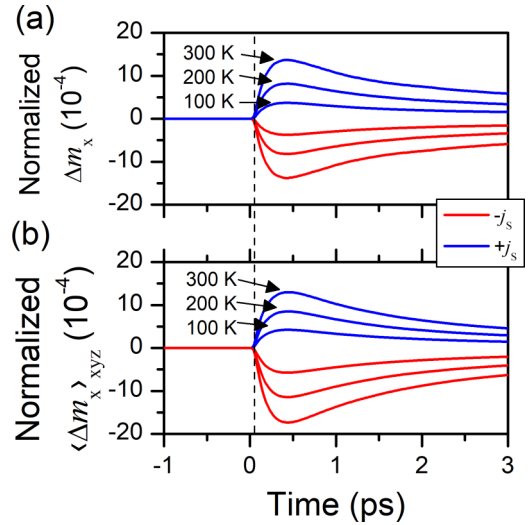


FIG. 8. Comparison of the spin dynamics according to the classical Hamiltonian model and to the numerical micromagnetic modeling. The red and blue lines are obtained for the opposite polarities of the spin current pulse. (a) Relative variations of averaged magnon number $\langle \Delta m_x \rangle$ from Eq. (A26) as a function of time, obtained from the Hamiltonian model given by Eq. (A21). Computation for different temperatures as indicated. (b) Corresponding micromagnetic simulation data, also shown in Fig. 6(c). The dashed line indicates the peak time of the injected spin current pulse.

in Eq. (A21) since those cancel out in the statistical average. Figure 8 shows the results obtained for positive and negative spin current pulses of equal magnitude, at three different temperatures. The data look quite similar to those shown in Fig. 6(c) in the main text. For instance, for positive spin injection, after a fast initial increase which saturates 350 fs after the maximum of the injection density, the magnon numbers decrease approximately exponentially with a decay time of 1.48(1) ps. This value is quite close to the one obtained in the numerical simulations [1.79(1) ps]. Small differences in decay time and in the overall magnitude can be attributed to the fact that in the rate equations (A21) interactions between the magnons are not taken into account. In contrast, in the micromagnetic simulation, the underlying fully nonlinear Landau-Lifshitz equation captures these processes. Also, slightly different compositions of the magnon ensembles in the analytic and numerical description can give rise to different decay rates.

[1] E. Beaurepaire, J.-C. Merle, A. Daunois, and J.-Y. Bigot, *Phys. Rev. Lett.* **76**, 4250 (1996).
[2] A. Kirilyuk, A. V. Kimel, and T. Rasing, *Rev. Mod. Phys.* **82**, 2731 (2010).
[3] J. M. Kikkawa and D. D. Awschalom, *Phys. Rev. Lett.* **80**, 4313 (1998).
[4] J.-Y. Bigot, M. Vomir, and E. Beaurepaire, *Nat. Phys.* **5**, 515 (2009).
[5] M. van Kampen, C. Jozsa, J. T. Kohlhepp, P. LeClair, L. Lagae, W. J. M. de Jonge, and B. Koopmans, *Phys. Rev. Lett.* **88**, 227201 (2002).

[6] T. Satoh, Y. Terui, R. Moriya, B. A. Ivanov, K. Ando, E. Saitoh, T. Shimura, and K. Kuroda, *Nat. Photonics* **6**, 662 (2012).
[7] Y. Au, M. Dvornik, T. Davison, E. Ahmad, P. S. Keatley, A. Vansteenkiste, B. Van Waeyenberge, and V. V. Kruglyak, *Phys. Rev. Lett.* **110**, 097201 (2013).
[8] I. Razdolski, A. Alekhin, N. Ilin, J. P. Meyburg, V. Roddatis, D. Diesing, U. Bovensiepen, and A. Melnikov, *Nat. Commun.* **8**, 15007 (2017).
[9] M. L. M. Lallieu, P. L. J. Helgers, and B. Koopmans, *Phys. Rev. B* **96**, 014417 (2017).

- [10] E. H. Frei, S. Shtrikman, and D. Treves, *Phys. Rev.* **106**, 446 (1957).
- [11] D. Berkov and J. Miltat, *J. Magn. Magn. Mater.* **320**, 1238 (2008).
- [12] M. Djordjevic and M. Münzenberg, *Phys. Rev. B* **75**, 012404 (2007).
- [13] B. Lenk, H. Ulrichs, F. Garbs, and M. Münzenberg, *Phys. Rep.* **507**, 107 (2011).
- [14] R. Hertel, W. Wulfhekel, and J. Kirschner, *Phys. Rev. Lett.* **93**, 257202 (2004).
- [15] V. V. Kruglyak, S. O. Demokritov, and D. Grundler, *J. Phys. D: Appl. Phys.* **43**, 264001 (2010).
- [16] S.-K. Kim, *J. Phys. D: Appl. Phys.* **43**, 264004 (2010).
- [17] J. Iwasaki, M. Mochizuki, and N. Nagaosa, *Nat. Nanotechnol.* **8**, 742 (2013).
- [18] M. Dvornik, Y. Au, and V. V. Kruglyak, Micromagnetic simulations in magnonics, in *Magnonics: From Fundamentals to Applications*, edited by S. O. Demokritov and A. N. Slavin (Springer, Berlin, Heidelberg, 2013), pp. 101–115.
- [19] H. Ulrichs, V. E. Demidov, and S. O. Demokritov, *Appl. Phys. Lett.* **104**, 042407 (2014).
- [20] C. Banerjee, P. Gruszecki, J. W. Klos, O. Hellwig, M. Krawczyk, and A. Barman, *Phys. Rev. B* **96**, 024421 (2017).
- [21] G. Malinowski, F. Dalla Longa, J. H. H. Rietjens, P. V. Paluskar, R. Huijink, H. J. M. Swagten, and B. Koopmans, *Nat. Phys.* **4**, 855 (2008).
- [22] M. Battiato, K. Carva, and P. M. Oppeneer, *Phys. Rev. Lett.* **105**, 027203 (2010).
- [23] P. Balaz, M. Zonda, K. Carva, P. Maldonado, and P. M. Oppeneer, *J. Phys.: Condens. Matter* **30**, 115801 (2018).
- [24] V. E. Demidov, S. Urazhdin, E. R. J. Edwards, M. D. Stiles, R. D. McMichael, and S. O. Demokritov, *Phys. Rev. Lett.* **107**, 107204 (2011).
- [25] H. A. Mook and R. M. Nicklow, *Phys. Rev. B* **7**, 336 (1973).
- [26] C. Etz, L. Bergqvist, A. Bergman, A. Taroni, and O. Eriksson, *J. Phys.: Condens. Matter* **27**, 243202 (2015).
- [27] A. Vansteenkiste, J. Leliaert, M. Dvornik, M. Helsen, F. Garcia-Sanchez, and B. V. Waeyenberge, *AIP Adv.* **4**, 107133 (2014).
- [28] A. Alekhin, I. Razdolski, N. Ilin, J. P. Meyburg, D. Diesing, V. Roddatis, I. Rungger, M. Stamenova, S. Sanvito, U. Bovensiepen, and A. Melnikov, *Phys. Rev. Lett.* **119**, 017202 (2017).
- [29] J. Slonczewski, *J. Magn. Magn. Mater.* **159**, L1 (1996).
- [30] M. A. Zimmeler, B. Özyilmaz, W. Chen, A. D. Kent, J. Z. Sun, M. J. Rooks, and R. H. Koch, *Phys. Rev. B* **70**, 184438 (2004).
- [31] C. Abert, H. Sepehri-Amin, F. Brückner, C. Vogler, M. Hayashi, and D. Suess, *Phys. Rev. Applied* **7**, 054007 (2017).
- [32] A. Melnikov, I. Razdolski, T. O. Wehling, E. T. Papaioannou, V. Roddatis, P. Fumagalli, O. Aktsipetrov, A. I. Lichtenstein, and U. Bovensiepen, *Phys. Rev. Lett.* **107**, 076601 (2011).
- [33] M. Battiato and K. Held, *Phys. Rev. Lett.* **116**, 196601 (2016).
- [34] G.-M. Choi and D. G. Cahill, *Phys. Rev. B* **90**, 214432 (2014).
- [35] See Supplemental Material at <http://link.aps.org/supplemental/10.1103/PhysRevB.98.054429> for animated graphs showing the simulated dynamics.
- [36] B. A. Kalinikos and A. N. Slavin, *J. Phys. C: Solid State Phys.* **19**, 7013 (1986).
- [37] J. Zak, E. Moog, C. Liu, and S. Bader, *J. Magn. Magn. Mater.* **89**, 107 (1990).
- [38] E. Turgut, C. La-o-vorakiat, J. M. Shaw, P. Grychtol, H. T. Nembach, D. Rudolf, R. Adam, M. Aeschlimann, C. M. Schneider, T. J. Silva, M. M. Murnane, H. C. Kapteyn, and S. Mathias, *Phys. Rev. Lett.* **110**, 197201 (2013).
- [39] R. F. L. Evans, D. Hinzke, U. Atxitia, U. Nowak, R. W. Chantrell, and O. Chubykalo-Fesenko, *Phys. Rev. B* **85**, 014433 (2012).
- [40] H. Suhl, *J. Phys. Chem. Solids* **1**, 209 (1957).
- [41] V. S. L'vov, *Wave Turbulence Under Parametric Excitation* (Springer-Verlag, Berlin, Heidelberg, Germany, 1994).
- [42] S. M. Rezende, F. M. de Aguiar, and A. Azevedo, *Phys. Rev. Lett.* **94**, 037202 (2005).
- [43] A. N. Slavin and P. Kabos, *IEEE Trans. Magn.* **41**, 1264 (2005).
- [44] A. Slavin and V. Tiberkevich, *Phys. Rev. Lett.* **95**, 237201 (2005).
- [45] V. E. Demidov, S. Urazhdin, H. Ulrichs, V. Tiberkevich, A. Slavin, D. Baither, G. Schmitz, and S. O. Demokritov, *Nat. Mater.* **11**, 1028 (2012).
- [46] A. Gurevich and G. Melkov, *Magnetization Oscillations and Waves* (CRC Press, Boca Raton, US, 1996).